

Multifunctional GdVO₄:Eu Core-Shell Nanoparticles Containing ²²⁵Ac for Targeted Alpha Therapy and Molecular Imaging*

M. Toro-González,^a R. Copping,^b S. Mirzadeh,^b J. V. Rojas^a

Abstract

Gadolinium vanadate nanoparticles (NPs) doped with europium, in concentrations between 5%–40%, were synthesized via an aqueous route to prove their multimodal imaging functionalities and their performance as radionuclide carriers for targeted alpha therapy. Core-shell Gd_{0.8}Eu_{0.2}VO₄ NPs were doped with the α -emitting actinium-225 to assess the *in vitro* retention of ²²⁵Ac and its decay daughters; francium-221 and bismuth-213. Gd_{0.8}Eu_{0.2}VO₄ core-shell NPs were obtained using a precipitation synthesis route having a tetragonal system, a spherical morphology, and a uniform particle size distribution. Gd_{0.8}Eu_{0.2}VO₄ core-shell NPs displayed the characteristic intense emission at 618 nm (red) and paramagnetic behavior of Eu and Gd cations, respectively. Partial retention of radionuclides was obtained with Gd_{0.8}Eu_{0.2}VO₄ core NPs, while deposition of two nonradioactive Gd_{0.8}Eu_{0.2}VO₄ shells significantly decreased the leakage of both ²²⁵Ac and ²²¹Fr. The luminescence and magnetic functionalities as well as radionuclide retention capabilities of Gd_{0.8}Eu_{0.2}VO₄ core-shell NPs demonstrate their potential for biomedical applications.

Keywords

Actinium-225, francium-221, bismuth-213, multifunctional nanoparticles, targeted alpha therapy, gadolinium and europium vanadate

1. Introduction

The development of nanomaterials for medical applications has experienced a continuous growth thanks to their unique physical and chemical properties.¹ In addition, modification of nanomaterials' surfaces with specific moieties to target particular diseases makes them suitable for theranostic applications.^{1,2} Complex pathophysiological processes can be studied by multiple molecular imaging techniques, such as fluorescence and magnetic resonance imaging (MRI), using a single multifunctional nanomaterial as a contrast agent.^{2–4} Similarly, the specific treatment of diseased cells can be achieved by combining anti-cancer drugs or radioisotopes with nanomaterials.⁵ Overall, nanomaterials have the potential to transform the treatment of diseases such as cancer in a more specific and efficient way compared to current procedures.⁶ For

* This manuscript has been authored by UT-Battelle, LLC, under contract DE-AC05-00OR22725 with the US Department of Energy (DOE). The US government retains and the publisher, by accepting the article for publication, acknowledges that the US government retains a nonexclusive, paid-up, irrevocable, worldwide license to publish or reproduce the published form of this manuscript, or allow others to do so, for US government purposes. DOE will provide public access to these results of federally sponsored research in accordance with the DOE Public Access Plan (<http://energy.gov/downloads/doe-public-access-plan>).

^a Department of Mechanical and Nuclear Engineering, Virginia Commonwealth University, Richmond, VA, United States. E-mail: torogonzalezm@vcu.edu (M. Toro González), jvrojas@vcu.edu (J. V. Rojas).

^b Nuclear Security and Isotope Technology Division, Oak Ridge National Laboratory, Oak Ridge, TN, United States. E-mail: coppingr@ornl.gov (R. Copping), mirzadehs@ornl.gov (S. Mirzadeh).

example, polymeric micelles,^{7,8} polymersomes,^{9,10} dendrimers,¹¹ quantum dots,^{12–14} gold nanoparticles (NPs),¹⁵ superparamagnetic iron oxides NPs,¹⁶ and lanthanide-based nanomaterials^{3,17} are among various nanomaterials that have shown promising capabilities for theranostic applications.

The development of lanthanide-based nanomaterials for theranostic applications has been remarkably active among these research fields due to their distinctive luminescence and magnetic properties and their low cytotoxicity.^{18–20} Characteristic luminescence properties of lanthanide ions encompass narrow emission lines, high photostability, an intense luminescence from ultraviolet (UV) to near-infrared, and multicolor emission, among others.^{18,19} Additionally, the electronic configuration of lanthanide ions ($\text{Ln}^{3+} = [\text{Xe}]4f^{n-1}5d^{0-1}6s^2$, $n = 1-15$) gives unique paramagnetic properties based on the unpaired electrons from the $4f$ orbitals.²⁰ Among lanthanides, Eu^{3+} and Gd^{3+} ions have been extensively studied because of the intense emission of Eu^{3+} at 618 nm wavelength (red) and the seven unpaired electrons of Gd^{3+} , which make them suitable for fluorescence and magnetic resonance imaging, respectively.²¹ The combination of both lanthanide ions has been the basis for the development and characterization of most bifunctional contrast agents.^{3,22–26} To illustrate, Nuñez *et al.* studied the europium doping level, from 2%–15%, within Eu-doped GdVO_4 nanocrystals functionalized with amino-dextran polymers and polyacrylic acid to assess their response as *in vitro* fluorescence and magnetic resonance imaging contrast agents.²⁷ The nanocrystals without functionalization showed the highest emission at 10% Eu^{3+} content with a partial quenching of the emission bands after functionalization with polyacrylic acid.²⁷ These functionalized nanocrystals exhibited negligible toxicity to epithelial cells based on the MTT [3-(4,5-dimethylthiazol-2-yl)-2,5-diphenyltetrazolium bromide] assays for concentrations up to 0.5 mg mL^{-1} and a negative (T_2 -weighted) MRI response.²⁷ Similarly, $\text{Gd}_{0.6}\text{Eu}_{0.4}\text{VO}_4$ NPs 5 nm and 30 nm in diameter were evaluated as sensors of reactive oxygen species and as both fluorescence and magnetic resonance imaging contrast agents.³ Both the small and large NPs showed a positive (T_1 -weighted) MRI response and the ability to quantitatively detect the concentration of reactive oxygen species inside living organisms.³ Toxicity studies revealed that 25% of the endothelial progenitor cells died after overnight incubation with the larger NPs, whereas the smaller NPs did not display cytotoxicity.³

Lanthanide-based NPs have also been studied as carriers for either drugs or radioisotopes toward targeted therapy.^{20,26,36,28–35} For example, Sm_2O_3 and Gd_2O_3 nanosheets doped with Eu^{3+} ions were studied as a promising pH-controlled anti-cancer drug carrier.³⁶ Similarly, Kim *et al.* evaluated the application of $\text{GdVO}_4:\text{Eu}$ NPs coated with mesoporous silica for anti-cancer drug delivery and molecular imaging.²⁶ Lanthanide-based core and core-shell NPs have shown promising capabilities for the retention of radioisotopes such as ^{89}Zr , ^{141}Ce , and ^{111}In for diagnostic applications^{37–39} and those that decay by multiple emission of α -particles, such as ^{225}Ac and ^{223}Ra , for targeted alpha therapy (TAT).^{29–33} The retention of decay daughters within the NPs has been shown to be dependent on the number of shells and their elemental composition.^{29,32} To illustrate, the retention of ^{221}Fr (first α -decay daughter of ^{225}Ac) was ~50% within LaPO_4 core NPs,³⁰ while an increase to 60% retention was achieved in $\text{La}_{0.5}\text{Gd}_{0.5}\text{PO}_4$ core NPs.³² The higher retention of ^{221}Fr for the latter was attributed to the greater electron density of Gd^{3+} with respect to La^{3+} . Nonetheless, the leakage of ~50% of ^{221}Fr would compromise the treatment efficacy and may result in renal toxicity from ^{213}Bi (the second α -decay daughter of

^{221}Fr).³² Therefore, nonradioactive shells with the same or different elemental composition to that of the core NPs were studied as barriers to enhance the retention of decay daughters. It was found that the deposition of two shells of $\text{La}_{0.5}\text{Gd}_{0.5}\text{PO}_4$ and a gold shell increases the retention of ^{221}Fr to 70%.³² Furthermore, the deposition of four shells of LaPO_4 or GdPO_4 accompanied by a layer of gold further increased the retention of ^{221}Fr to 80% and 90%, respectively.³² Analogously, it has been reported that >99.9% of ^{223}Ra can be retained within LaPO_4 core + 2 shells NPs while ^{211}Pb is retained quantitatively.²⁹

In this work, we studied the multifunctional capabilities of $\text{Gd}_{0.8}\text{Eu}_{0.2}\text{VO}_4$ core and core + 2 shells NPs for molecular imaging and TAT. First, we developed a procedure for the synthesis of core-shell structures and assessed the deposition of shells based on the particle growth. The luminescence and magnetic properties of both core and core-shell NPs were characterized to evaluate their potential application as fluorescence and magnetic resonance imaging contrast agents. Lanthanide-doped GdVO_4 NPs have shown to be promising phosphors because of their moderate cut-off phonon energy,⁴⁰ high thermal conductivity and chemical stability,⁴¹ and ability to host different lanthanides.^{40,42,43} The lower phonon energy of GdVO_4 (805 cm^{-1})⁴⁴ makes them more attractive for the development of up-conversion phosphors with respect to LnPO_4 hosts ($\sim 1000\text{ cm}^{-1}$).⁴⁵ Although GdVO_4 has a higher phonon energy relative to that of NaREF_4 ,⁴⁵ the synthesis of rare earth fluorides requires complicated and multi-step procedures in which either environmentally harmful organic solvents, high temperatures, and/or protective atmospheres are used.^{46–49} Despite the fact that lanthanide-doped LaVO_4 ^{50–52} and LuVO_4 ⁵³ may provide greater luminescence intensity to that of GdVO_4 , the presence of Gd cations in $\text{GdVO}_4:\text{Ln}$ NPs will allow their application in MRI for multimodal molecular imaging. In addition to exploring the multifunctional capabilities of Eu-doped GdVO_4 for molecular imaging, we tested the ability of both $\text{Gd}_{0.8}\text{Eu}_{0.2}\text{VO}_4$ core and core + 2 shells NPs to host and retain ^{225}Ac , ^{221}Fr , and ^{213}Bi *in vitro* towards TAT. Lanthanide vanadate NPs are a promising alternative for the retention of radionuclides toward biomedical applications since vanadate ceramics have proven to be resistant to radiation damage.⁵⁴ Moreover, monodisperse LnVO_4 NPs can be synthesized using an aqueous route in a relatively short time (<1 hour),^{3,55} which may promote their use for the retention of diagnostic and/or therapeutically relevant short-lived radionuclides. Overall, this study demonstrates the potential application of lanthanide vanadate NPs as theranostic platforms for molecular imaging and targeted radionuclide therapy.

2. Experimental

2.1. Materials

Gadolinium(III) chloride hexahydrate ($\text{GdCl}_3 \cdot 6\text{H}_2\text{O}$, 99.9%, trace metal basis) and sodium citrate dihydrate ($\text{Na}_3\text{C}_6\text{H}_5\text{O}_7 \cdot 2\text{H}_2\text{O}$, ultrapure bioreagent) were obtained from Sigma Aldrich. Europium(III) chloride hexahydrate ($\text{EuCl}_3 \cdot 6\text{H}_2\text{O}$, 99.9%, trace metal basis) and sodium orthovanadate (Na_3VO_4 , 99%) were purchased from Acros Organics. Bismuth(III) chloride (BiCl_3 , 99.9%) was obtained from Alfa Aesar. A MilliQ® water purification system was used to obtain deionized (DI) water (18 M Ω). All chemicals were used without further purification. The pH of Na_3VO_4 was adjusted to 12.5 using NaOH (1 M). Biotech regenerated cellulose membrane with an 8–10 kDa molecular weight cutoff was purchased from Spectra®. The dialysis membrane was washed several times with DI water to remove preservatives. Standards for inductively

coupled plasma (ICP) of gadolinium and bismuth (1000 ppm) were obtained from Inorganic VenturesTM. A carrier-free ²²⁵Ac stock was acquired from a mixture of ²²⁸Th, ²²⁹Th, and ²³²Th by anion and cation exchange chromatography at Oak Ridge National Laboratory.⁵⁶

2.2. Synthesis of GdVO₄:Eu core and core-shell NPs

Europium-doped gadolinium vanadate (GdVO₄:Eu) core and core-shell NPs were synthesized by an aqueous route at moderate temperature (60°C) from a mixture of lanthanide chloride salts, sodium citrate, and sodium orthovanadate.⁵⁵ The synthesis of GdVO₄:Eu core NPs started by mixing GdCl₃·6H₂O (0.1 M) and EuCl₃·6H₂O (0.1 M) at specific volume ratios [Eu/(Gd+Eu) = 0.05, 0.1, 0.2, and 0.4]. Next, a 0.75 volume equivalent of Na₃C₆H₅O₇·2H₂O (0.1 M) was added to a 1 volume equivalent of the lanthanide solution. The resulting mixture was homogenized using a vortex mixer until a white solution was obtained. Lastly, a 0.75 volume equivalent of Na₃VO₄ (0.1 M) was added and the solution was agitated until it was clear and colorless. The solution was heated at 60°C for 30 minutes to synthesize GdVO₄:Eu core NPs; afterwards the suspension was allowed to cool to room temperature. Simultaneously, a solution having the same chemical composition to that used for the synthesis of the core NPs was prepared following the procedure previously described. This solution was then added in a volume ratio of 1.5:1 to the synthesized GdVO₄:Eu core NPs suspension and mixed thoroughly using a vortex mixer. The resulting clear and colorless suspension was subsequently heated at 60°C for 30 minutes to synthesize GdVO₄:Eu core + 1 shell NPs. The deposition of the second shell was carried out by repeating this procedure while keeping the volume ratio of 1.5:1 between the fresh lanthanide-citrate-vanadate solution and the core NPs suspension.

2.3. Synthesis of ²²⁵Ac-doped GdVO₄:Eu core and core-shell NPs

The synthesis of Gd(²²⁵Ac)VO₄:Eu core and core-shell NPs was performed following an analogous procedure to that described for the nonradioactive core and core-shell NPs with the addition of ²²⁵Ac during the synthesis of the core. An aliquot containing ~50 μCi of ²²⁵Ac diluted in 0.1 M HNO₃ was initially evaporated to dryness on a glass conical vial at 80°C. Subsequently, a mixture of lanthanide chloride was added into the vial and stirred for 5 minutes to ensure a homogeneous dispersion of ²²⁵Ac cations and decay daughters in solution. The addition of sodium citrate and sodium orthovanadate was done as described for the nonradioactive core. The synthesis of core Gd(²²⁵Ac)VO₄:Eu and the deposition of shells were completed as described in the previous section. Both Gd(²²⁵Ac)VO₄:Eu core and core + 2 shells NPs suspensions were transferred into dialysis membranes and dialyzed against DI water to remove unreacted species and evaluate the radiochemical yield and retention of radionuclides within the NPs over time.

2.4. Materials characterization

Characterization was carried out on nonradioactive NPs. The crystal structure of GdVO₄:Eu core and core-shell NPs was characterized by powder x-ray diffraction using a Panalytical X'Pert Pro x-ray diffractometer. The diffractometer was operated at 45 kV and 40 mA with a copper anode (Cu k_α, λ = 1.504 Å). For the sample preparation, the as-prepared core and core-shell suspensions were mixed with ethanol in a 3:2 volume ratio to promote the precipitation of the NPs. Subsequently, the core and core-shell NPs were collected by centrifugation and dried

in an oven at 60°C for 18 hours. The dried samples were ground using a mortar and pestle until a fine powder was obtained. The hydrodynamic size of the GdVO₄:Eu NPs was evaluated from the as-prepared suspensions by dynamic light scattering using a NanoPlus HD (Micromeritics®). This equipment uses a laser diode operated at 30 mW and 660 nm wavelength. The morphology of the NPs was assessed using transmission electron microscopy (TEM) in a Zeiss Libra® 120 with a LaB₆ filament operating at 120 kV and a FEI Titan operating at 300 kV. The sample preparation consisted in drop-casting diluted core and core + 2 shells NPs suspensions (×75 in DI water) onto a 300 mesh formvar/carbon copper grid. Vibrating sample magnetometry was used to record the magnetic moment of the GdVO₄:Eu core and core-shell NPs. Each powder sample was massed into a polypropylene capsule, centered, and measured in a field of -30000–30000 Oe at 300 K in a Versalab™ 3 Tesla. Absorption, excitation, and emission spectra were collected in a Thermo Scientific™ GENESYS 10S UV-Vis spectrophotometer and a Varian Eclipse fluorescence spectrophotometer. The as-prepared GdVO₄:Eu core and core-shell suspensions were diluted in DI water while the multiple spectra were collected using a quartz cuvette (10 mm pathlength) with four optically clear sides. Time-resolved luminescence lifetimes were recorded using a QuantMaster-3 spectrofluorometer with a Xenon Flash lamp excitation source and a photomultiplier tube (PMT) detector. The relative concentration of lanthanide ions was assessed by energy-dispersive x-ray spectroscopy using a Hitachi SU-70 field emission scanning electron microscope. The chemical yield of GdVO₄:Eu core and core-shell NPs was assessed by inductively coupled plasma–optical emission spectroscopy (ICP-OES) using nonradioactive suspensions and an Agilent 5110 ICP-OES with a minimum detection limit for Gd of 2.5 ppb. After synthesis, a 1.5 mL aliquot of the suspension was dialyzed for 15 hours against 200 mL of DI water. The chemical yield was calculated from measuring the concentration of Gd cations in both dialysate and dialyzed suspension. A calibration curve, obtained by the successive dilution of a 1000 ppm Gd ICP standard between 0.1–100 ppm, was used to determine the concentration of Gd cations in each suspension.

2.5. Radiochemical yield of ²²⁵Ac doped NPs and retention of ²²⁵Ac, ²²¹Fr, and ²¹³Bi

Radiochemical yield of ²²⁵Ac and retention of ²²⁵Ac, ²²¹Fr, and ²¹³Bi were evaluated *in vitro* by dialyzing the as-prepared Gd(²²⁵Ac)VO₄:Eu core and core + 2 shells suspensions against DI water. After synthesis, both suspensions were dialyzed for 18 hours to remove unreacted species. A sample from the dialysate was analyzed to determine the fraction of radionuclides that did not react during the NPs synthesis. Subsequently, this dialysate was replaced with clean DI water to assess the retention of ²²⁵Ac, ²²¹Fr, and ²¹³Bi over time. A 5 mL aliquot from the dialysate was taken periodically over a period of 4 weeks and counted in a high-purity germanium detector to determine the activity of the radionuclides. In the case of short half-life ²²¹Fr ($T_{1/2} = 4.8$ minutes), the time elapsed between the withdrawal of the aliquot and the start of the measurement was recorded. The assay of each aliquot consisted of 20 consecutive 1-minute interval measurements that were used to construct the decay curve of ²²¹Fr. The same aliquot was analyzed the following day to assess the level of activity of ²²⁵Ac based on the ²²¹Fr activity now in equilibrium with actinium. The γ -energy and intensities used for the evaluation of the activity of ²²⁵Ac, ²²¹Fr, and ²¹³Bi were 150.1 keV (0.6%), 218.1 keV (11.4%), and 440.4 keV (25.9%), respectively. All measurements were corrected for radioactive decay and volume loss due to the aliquots withdrawn for the analysis. The high-purity germanium detector had a crystal active volume of ~100 cm³ and a beryllium window and was coupled to a PC-based multichannel

analyzer (Canberra Industries, Meriden, CT). Energy and efficiency calibrations were determined by γ -ray sources traceable to the National Institute of Standards and Technology.

3. Results

3.1. Synthesis of GdVO₄:Eu core and core-shell NPs

GdVO₄:Eu core and core-shell NPs were synthesized by precipitation of Ln³⁺ and [VO₄]³⁻ ions in aqueous media using sodium citrate as complexing agent.⁵⁵ The formation of GdVO₄:Eu core NPs begins with lanthanide-citrate-vanadate oligomeric species, as shown in Fig. 1(a). Upon heating, these species decompose causing the formation of citrate ions and promoting the interaction between Ln³⁺ and [VO₄]³⁻ ions. This interaction results in the formation of GdVO₄:Eu nuclei [Fig. 1(b)], which continuously grow to form GdVO₄:Eu core NPs.⁵⁷ The stabilization of the GdVO₄:Eu NPs is achieved through complexation between citrate and Ln³⁺ ions on the NPs' surface [Fig. 1(c)].⁵⁵ Thus, it is critical to have a higher concentration of Ln³⁺ ions with respect to [VO₄]³⁻, as defined by the volume ratio used during the synthesis. The deposition of the first shell begins with the mixing of the GdVO₄:Eu core NPs suspension with a solution containing lanthanide-citrate-vanadate oligomeric species [Fig. 1(d)]. This mixture is heated at 60°C for 30 minutes to promote the decomposition of the oligomeric species and the formation of GdVO₄:Eu nuclei, as described previously for the core NPs. The shell growth on the GdVO₄:Eu core surface might be explained by Ostwald ripening, where the smaller nuclei dissolve while the larger nuclei and/or core NPs coarsen.⁵⁸ This process is represented in Fig. 1(e) where small nuclei, denoted by small red spheres, are formed on the NPs' surface while only few larger nuclei reach an energetically stable size for the formation of new GdVO₄:Eu core NPs. This process continues until all small nuclei dissolve and coarsen on the core NPs' surface, resulting in the formation of core-shell NPs [Fig. 1(f)]. The red spheres shown in Fig. 1(f) correspond to GdVO₄:Eu core NPs formed during the deposition of shells onto the core NPs. The GdVO₄:Eu core-shell NPs as well as the core NPs are stabilized through complexation between Ln³⁺ and citrate ions.

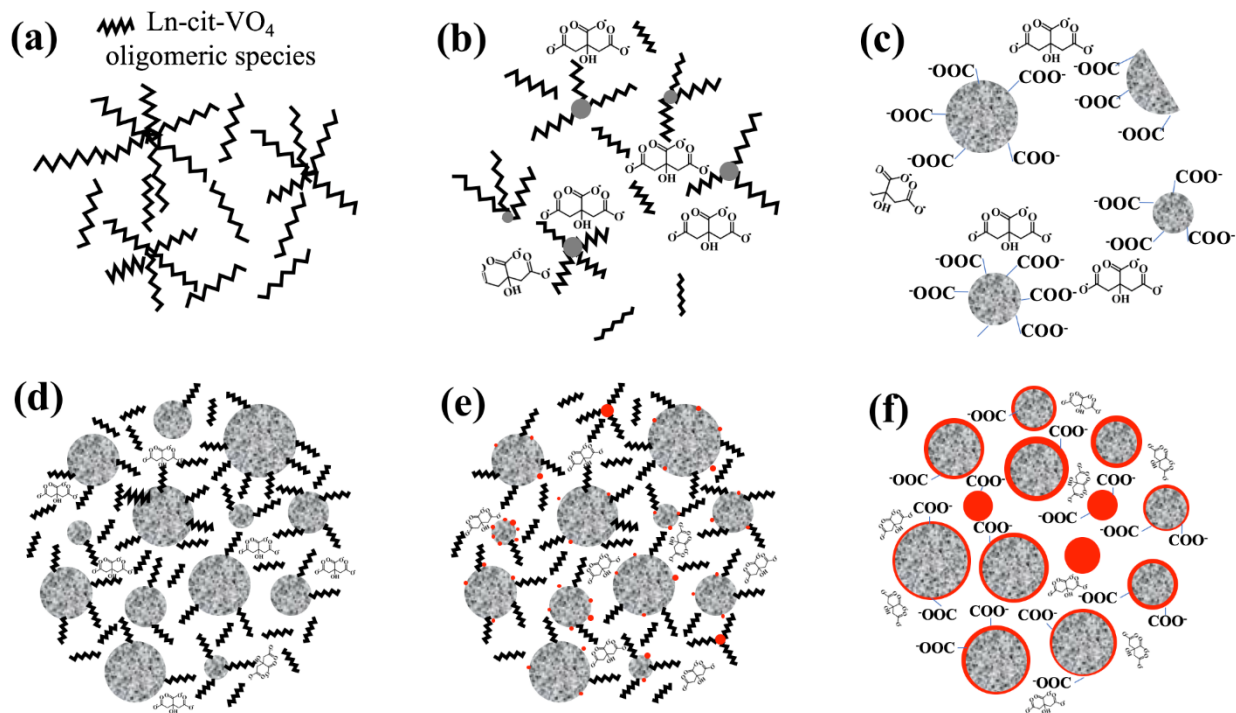


Fig. 1 Schematic representation of LnVO_4 core and core-shell NPs formation

For the development of a bimodal platform with fluorescence and magnetic resonance imaging capabilities, core NPs with Eu^{3+} concentrations of either 5%, 10%, 20%, or 40% were synthesized as described in the experimental section. The diffraction patterns, absorption, excitation, and emission spectra were collected for the different samples. As shown in Fig. S.1, core NPs have a tetragonal system with a zircon-type structure and space group $I4_1/amd$. The increase in Eu^{3+} concentration results in a slight shifting of 2θ , which implies a change in the d-spacing due to elastic strains imposed by the difference in size between the ionic radius of Gd^{3+} and Eu^{3+} ions. Furthermore, the variation in Eu^{3+} concentration does not affect the crystallite size of the $\text{GdVO}_4:\text{Eu}$ core NPs (Table S.1). The absorption, excitation, and emission spectra showed a higher intensity upon an increase in Eu^{3+} from 5% to 40%, as shown in Figs. S.2, S.3, and S.4. Nevertheless, the increase in the emission intensity reaches a maximum value $\sim 20\%$ (Fig. S.4). A 20% Eu^{3+} concentration was selected for the synthesis of core and core-shell NPs since it will provide the highest emission intensity with the minimum dopant concentration. As shown in Table S.2, the elemental composition of the synthesized NPs is in agreement with the input concentrations based on the energy-dispersive x-ray spectroscopy results.

3.2. Crystal structure

The diffraction patterns of $\text{Gd}_{0.8}\text{Eu}_{0.2}\text{VO}_4$ core and core-shell NPs are shown in Fig. 2. HighScore Plus software with a database from the International Centre for Diffraction Data was used to determine the crystal structure of each diffraction pattern. It was found that $\text{Gd}_{0.8}\text{Eu}_{0.2}\text{VO}_4$ core and core-shell NPs have a tetragonal system with a zircon-type structure and space group $I4_1/amd$, which corresponds in general to lanthanide vanadate (LnVO_4). The reference pattern of pure GdVO_4 (pdf: 00-017-0260) was selected for comparison of the different samples based on the relatively high concentration of Gd^{3+} ions and the similarity between the

ionic radii of both Ln^{3+} ions (94.7 and 93.8 pm for Eu^{3+} and Gd^{3+} , respectively).⁵⁹ The characteristic peak broadening caused by the nanometric size of the crystallites was observed for all diffraction patterns (Fig. 2). A slight decrease of the full width at half maximum of the peaks was observed upon deposition of $\text{Gd}_{0.8}\text{Eu}_{0.2}\text{VO}_4$ shells, which suggests an increase of the crystallite size. The peak located at 25° , which corresponds to the (200) plane in the tetragonal structure, represents the most intense reflection observed in the diffraction patterns. This peak was used to calculate the crystallite size (D) of $\text{Gd}_{(1-x)}\text{Eu}_x\text{VO}_4$ core and $\text{Gd}_{0.8}\text{Eu}_{0.2}\text{VO}_4$ core and core-shell NPs using the Debye-Scherrer equation ($D = 0.9\lambda/\beta \cos\theta$), where λ is the wavelength of the Cu-K α radiation, β is the full width at half maximum of the selected reflection, and θ is the Bragg angle. The crystallite size values obtained for the different samples are summarized in Table S.1 and Table 1. From these results it is observed that the deposition of two shells to the $\text{Gd}_{0.8}\text{Eu}_{0.2}\text{VO}_4$ core NPs results in an increase of the crystallite size from 4.7 to 5.6 nm (Table 1).

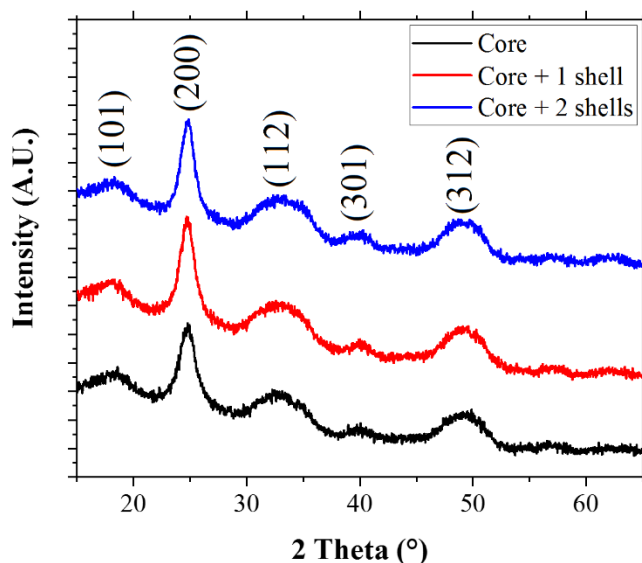


Fig. 2 Diffraction patterns of $\text{Gd}_{0.8}\text{Eu}_{0.2}\text{VO}_4$ core and core-shell NPs

Table 1 Summary of the crystallite size of $\text{Gd}_{0.8}\text{Eu}_{0.2}\text{VO}_4$ core and core-shell NPs

Sample	Crystallite size (nm)
Core	4.7
Core + 1 shell	5.1
Core + 2 shells	5.6

3.3. Morphology and particle size distribution

The morphology of nonradioactive $\text{Gd}_{0.8}\text{Eu}_{0.2}\text{VO}_4$ core and core-shell NPs was evaluated by TEM. Monodispersed $\text{Gd}_{0.8}\text{Eu}_{0.2}\text{VO}_4$ core NPs with spherical shape ranging from 2.0–5.1 nm have a mean particle size of 3.4 ± 0.7 nm, indicating a narrow particle size distribution [Fig. 3(a)]. $\text{Gd}_{0.8}\text{Eu}_{0.2}\text{VO}_4$ core + 2 shells NPs displayed spherical morphology with a mean particle size of 4.4 ± 1.0 nm [Fig. 3(b)]. The spacing between lattice fringes (~ 3.54 Å) is in agreement with the interplanar spacing d_{200} of GdVO_4 (~ 3.61 Å).

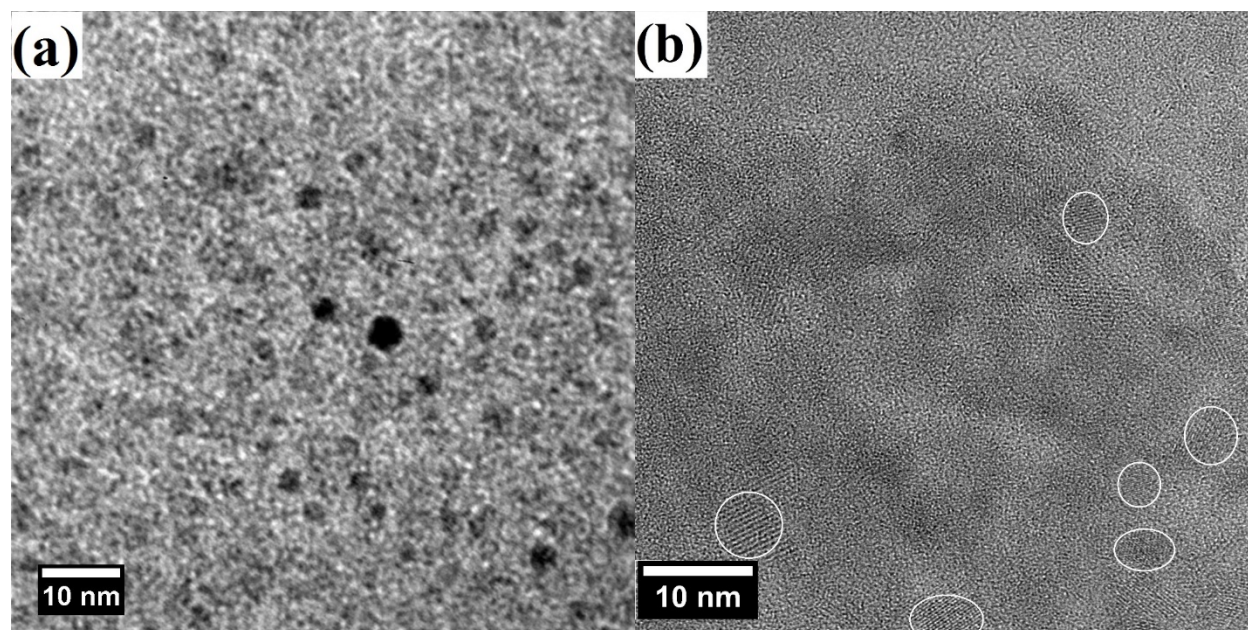


Fig. 3 High resolution TEM images of $Gd_{0.8}Eu_{0.2}VO_4$ (a) core and (b) core + 2 shells NPs

Dynamic light scattering was used to obtain the mean particle size and size distribution of $Gd_{0.8}Eu_{0.2}VO_4$ core and core-shell NPs based on the intensity and number distributions. The intensity and number distributions of both core and core-shell $Gd_{0.8}Eu_{0.2}VO_4$ NPs are shown in Fig. S.6. The deposition of shells caused an increase in the peak width and mean particle size of the particle size distribution by intensity and number (Fig. S.6). The polydispersity index, mean particle size, and standard deviation for the core and core-shell $Gd_{0.8}Eu_{0.2}VO_4$ NPs are summarized in Table 2. The low polydispersity index values of both core and core + 1 shell suspensions suggest the presence of highly monodisperse NPs in suspension (Table 2). As expected, the deposition of shells was accompanied by an increase in the PI and mean particle size based on both particle size distributions (Table 2).

Table 2 Statistics obtained from dynamic light scattering for $Gd_{0.8}Eu_{0.2}VO_4$ core and core-shell NPs

Sample	Polydispersity index	Mean size (nm)	
		Intensity Distribution	Number Distribution
Core	0.028	10.5 ± 3.6	6.2 ± 1.4
Core + 1 shell	0.053	14.5 ± 4.6	9.1 ± 2.1
Core + 2 shells	0.148	15.2 ± 3.1	12.1 ± 2.0

3.4. Magnetic susceptibilities

The mass magnetization as a function of the magnetic field for $Gd_{0.8}Eu_{0.2}VO_4$ core and core-shell NPs is shown in Fig. 4. A linear increase of the mass magnetization with the magnetic field, which corresponds to the characteristic paramagnetic response of Ln^{3+} at 300 K, was observed for $Gd_{0.8}Eu_{0.2}VO_4$ core and core-shell NPs (Fig. 4). The molar magnetic susceptibility

(χ_m) was calculated from the slope of this curve (Table S.3). The magnetic susceptibility of $\text{Gd}_{0.8}\text{Eu}_{0.2}\text{VO}_4$ core and core-shell NPs is $56 \times 10^{-6} \text{ emu Oe}^{-1} \text{ g}^{-1}$. These results are in agreement with the constant elemental composition of gadolinium and europium cations over $\text{Gd}_{0.8}\text{Eu}_{0.2}\text{VO}_4$ core and core-shell NPs and the Curie-Weiss Law that relates χ_m with the concentration and magnitude of the effective magnetic moment (μ_{eff}) associated to each Ln^{3+} .⁶⁰

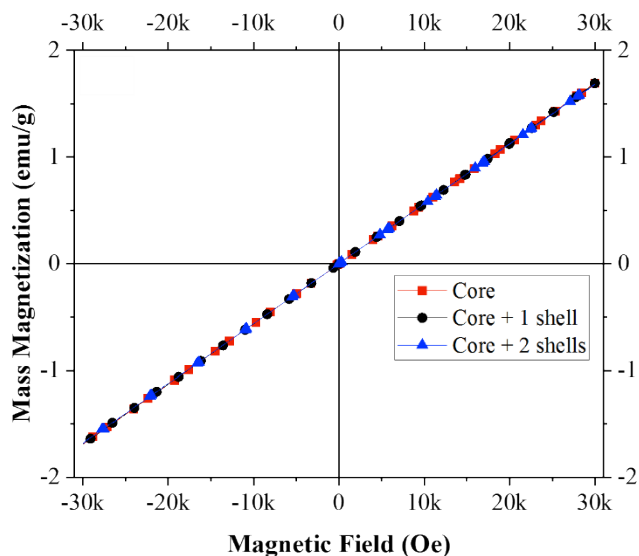


Fig. 4 Mass magnetization versus magnetic field of $\text{Gd}_{0.8}\text{Eu}_{0.2}\text{VO}_4$ core and core-shell NPs

3.5. Luminescence properties

Absorption, excitation, and emission spectra for $\text{Gd}_{(1-x)}\text{Eu}_x\text{VO}_4$ core and $\text{Gd}_{0.8}\text{Eu}_{0.2}\text{VO}_4$ core and core-shells are presented in Figs. S.2–S.4 and 5, respectively. The absorption spectrum is characterized by an absorption band around 280 nm, which corresponds to the $\text{V}^{5+}\text{-O}^{2-}$ charge transfer.⁴³ An increase in the elemental composition of Eu^{3+} resulted in a slight rise in the absorbance of the $\text{V}^{5+}\text{-O}^{2-}$ band (Fig. S.2), whereas the deposition of shells contributed to a significant increase in absorbance [Fig. 5(a)]. The excitation spectrum for the different samples was recorded using an emission wavelength of 618 nm, a PMT voltage of 600 V, and an excitation filter between 250–395 nm. As shown in Figs. 5(b) and S.3, the excitation spectrum is characterized by two excitation bands corresponding to $\text{Eu}^{3+}\text{-O}^{2-}$ (~280 nm) and $\text{V}^{5+}\text{-O}^{2-}$ (~305 nm) charge transfers, respectively.^{61–63} The band at ~305 nm is related to the symmetry-allowed absorption ${}^1\text{A}_1 \rightarrow {}^1\text{T}_2$ of the $[\text{VO}_4]^{3-}$ unit.⁶² Increment of Eu^{3+} elemental composition resulted in higher intensity for the $\text{Eu}^{3+}\text{-O}^{2-}$ band, while the $\text{V}^{5+}\text{-O}^{2-}$ band became unnoticeable due to overlapping between both bands (Fig. S.3). In contrast, the normalized intensity of the $\text{V}^{5+}\text{-O}^{2-}$ band increased upon the deposition of shells to the core NPs [Fig. 5 (b)]. Finally, the emission spectrum of each sample was recorded using an excitation wavelength of 280 nm, a PMT voltage of 600 V, and an emission filter from 295–1100 nm to prevent unwanted secondary order transmission.⁶⁴ All emission spectra displayed the characteristic ${}^5\text{D}_0 \rightarrow {}^7\text{F}_1$ ($J = 1-4$) emission bands of Eu^{3+} ions originating from low energy transfer (Figs. 5(c) and S.3).⁶⁵ It has been reported that the dopant concentration has to be optimized for each Ln^{3+} ion based on the properties of the host lattice.⁶⁶ Thus, a Eu^{3+} concentration of 20% was chosen for the synthesis of core-shell NPs based on its highest normalized intensity. The normalized intensity of

$\text{Gd}_{0.8}\text{Eu}_{0.2}\text{VO}_4$ has its maximum for the core NPs, and it then decreased upon successive deposition of shells. The inset in Fig. 5(c) corresponds to photographs taken of aliquots from $\text{Gd}_{0.8}\text{Eu}_{0.2}\text{VO}_4$ core and core-shell NPs suspensions under UV light ($\lambda = 254$ nm). The absolute quantum yields of $\text{Gd}_{(1-x)}\text{Eu}_x\text{VO}_4$ core and $\text{Gd}_{0.8}\text{Eu}_{0.2}\text{VO}_4$ core and core-shells NPs were calculated as reported elsewhere.^{67,68} The results indicate that increasing the Eu^{3+} concentration from 5% to 40% caused a decrease in quantum yield from 29.4% to 22.6% (Table S.5). Similarly, the deposition of 2 $\text{Gd}_{0.8}\text{Eu}_{0.2}\text{VO}_4$ shells decreased the quantum yield in $\sim 9\%$ with respect to core NPs (Table S.6). Time-resolved luminescence decay curves of $\text{Gd}_{(1-x)}\text{Eu}_x\text{VO}_4$ core NPs and $\text{Gd}_{0.8}\text{Eu}_{0.2}\text{VO}_4$ core-shell NPs are shown in Fig. S.7. The decay curves of both core and core-shell NPs displayed a better fit (higher R^2) when using a biexponential function with respect to that obtained with an exponential (Tables S.7 and S.8). An increase of Eu^{3+} concentration and the deposition of shells caused a decrease in the average luminescence decay lifetime, calculated according to Yaiphaba *et al.*⁶⁸

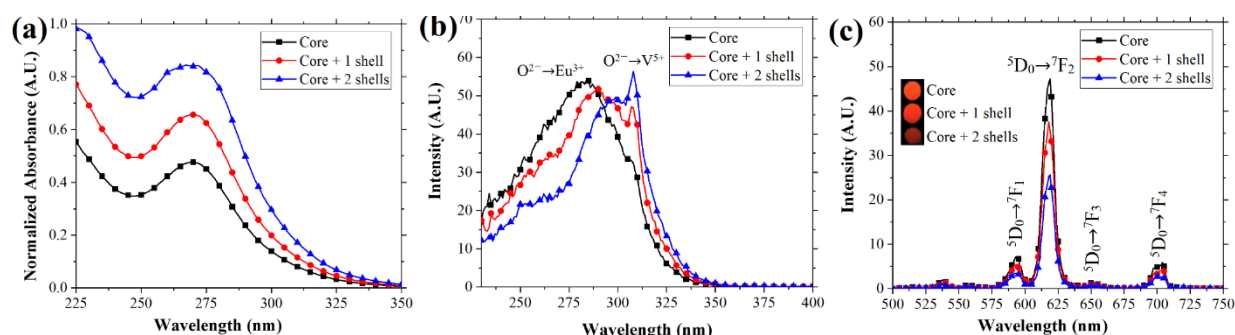


Fig. 5 (a) Absorption, (b) excitation ($\lambda_{\text{em}} = 618$ nm), and (c) emission ($\lambda_{\text{ex}} = 280$ nm) spectra of $\text{Gd}_{0.8}\text{Eu}_{0.2}\text{VO}_4$ core and core-shell NPs. Inset in Fig. 5(c) corresponds to pictures taken under UV light of the $\text{Gd}_{0.8}\text{Eu}_{0.2}\text{VO}_4$ core and core-shell suspensions ($\lambda = 254$ nm)

3.6. Chemical yield of $\text{GdVO}_4:\text{Eu}$ core and core-shell NPs

ICP-OES was utilized to measure the concentration of Gd cations in order to assess the chemical yield of $\text{Gd}_{0.8}\text{Eu}_{0.2}\text{VO}_4$ core and core-shell NPs. After NP synthesis the unreacted species, particularly Gd cations, were removed by dialysis, as described in the experimental section. The average chemical yield obtained from measuring the Gd concentration in the dialysate and dialyzed suspension is summarized in Table 3. The lowest Gd yield was obtained for $\text{Gd}_{0.8}\text{Eu}_{0.2}\text{VO}_4$ core NPs at $41.1 \pm 16.5\%$, whereas the deposition of shells increased the yield up to $\sim 55\%$ for both core + 1 and core + 2 shells. The Gd chemical yield of nonradioactive $\text{Gd}_{0.8}\text{Eu}_{0.2}\text{VO}_4$ core and core-shell NPs contributes to understanding the radioactivity losses observed during the synthesis of radionuclide-doped NPs.

Table 3 Average chemical yield of $\text{Gd}_{0.8}\text{Eu}_{0.2}\text{VO}_4$ core and core-shell NPs

Structure	Average chemical yield (%)
Core	41.1 ± 16.5
Core + 1 shell	55.4 ± 8.0
Core + 2 shells	54.8 ± 11.2

3.7. *In vitro* retention of ^{225}Ac and decay daughters

Retention of radioisotopes and decay daughters in biological constructs is a major challenge for the implementation of radioimmunotherapy and TAT for cancer treatment. The encapsulation of α -emitting radioisotopes is essential as daughter isotopes have the potential to increase overall general body dose and cause damage to healthy tissue if not retained at the tumor site.⁶⁹ Development of nano-carriers appears to be the most promising alternative among various approaches to deal with this challenge.⁶⁹ Thus, *in vitro* retention of ^{225}Ac and its decay daughters ^{221}Fr and ^{213}Bi was studied in $\text{Gd}_{0.8}\text{Eu}_{0.2}\text{VO}_4$ core and core + 2 shells NPs. Particularly, the release of ^{221}Fr and ^{213}Bi from the nano-carrier will cause unwanted radiotoxicity primarily to the kidneys as well as to other organs.⁶⁹ Figure 6 shows the fraction of radioactivity (leakage) found in the dialysate from ^{225}Ac as a function of time for both core and core + 2 shells. The activity of ^{225}Ac in the dialysate continuously increased until it reached a plateau, at which point the dialysate was replaced with fresh DI water to continue monitoring the release of ^{225}Ac . After changing the dialysate, the fraction of radioactivity of ^{225}Ac built up again and reached a maximum of $20 \pm 5\%$ for core and $2.7 \pm 0.5\%$ for core + 2 shells after 4 weeks (Fig. 6). At least 7 days were required to achieve a stable concentration of ^{225}Ac cations in the dialysate. Based on these results, the radiochemical yield of ^{225}Ac , calculated after taking the respective corrections for the activity lost during the synthesis and dialysis, was $58.3 \pm 14.1\%$ for core and $94.8 \pm 1.5\%$ for core + 2 shells. The former value is in agreement with the NPs chemical yield of $41.1 \pm 16.5\%$ measured using ICP-OES based on the concentration of unreacted Gd cations.

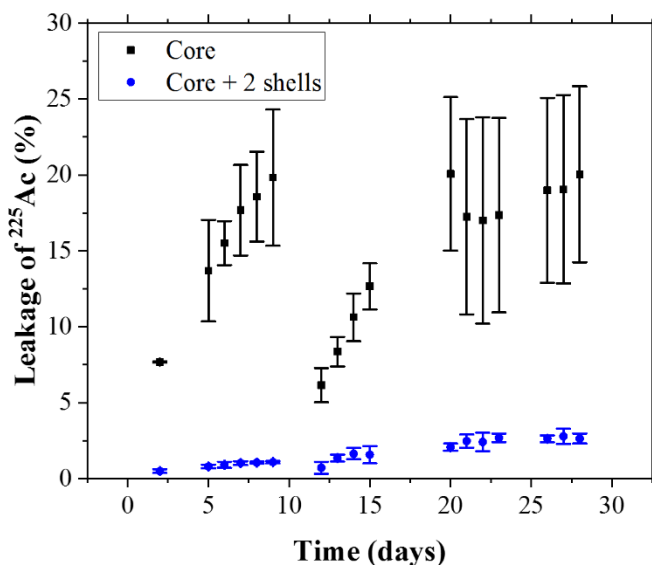


Fig. 6 Leakage of ^{225}Ac from $\text{Gd}_{0.8}\text{Eu}_{0.2}\text{VO}_4$ core and core + 2 shells NPs as a function of time

The leakage of ^{221}Fr and ^{213}Bi from the NPs was determined after subtracting the radioactivity of both radionuclides being produced from ^{225}Ac in the dialysate. The leakage of ^{221}Fr from $\text{Gd}_{0.8}\text{Eu}_{0.2}\text{VO}_4$ core NPs reached $55 \pm 3.6\%$ within 10 days and increased to $67.6 \pm 3.3\%$ after 28 days [Fig. 7(a)]. Leakage of ^{221}Fr from $\text{Gd}_{0.8}\text{Eu}_{0.2}\text{VO}_4$ core + 2 shells NPs was only $36.3 \pm 6.2\%$ in 10 days and gradually increased to a maximum value of $45.5 \pm 3.6\%$ [Fig. 7(b)]. The leakage of ^{213}Bi was found to be $<15\%$ for core NPs, while it reached a maximum of $\sim 22\%$ for core + 2 shells NPs (Fig. 7).

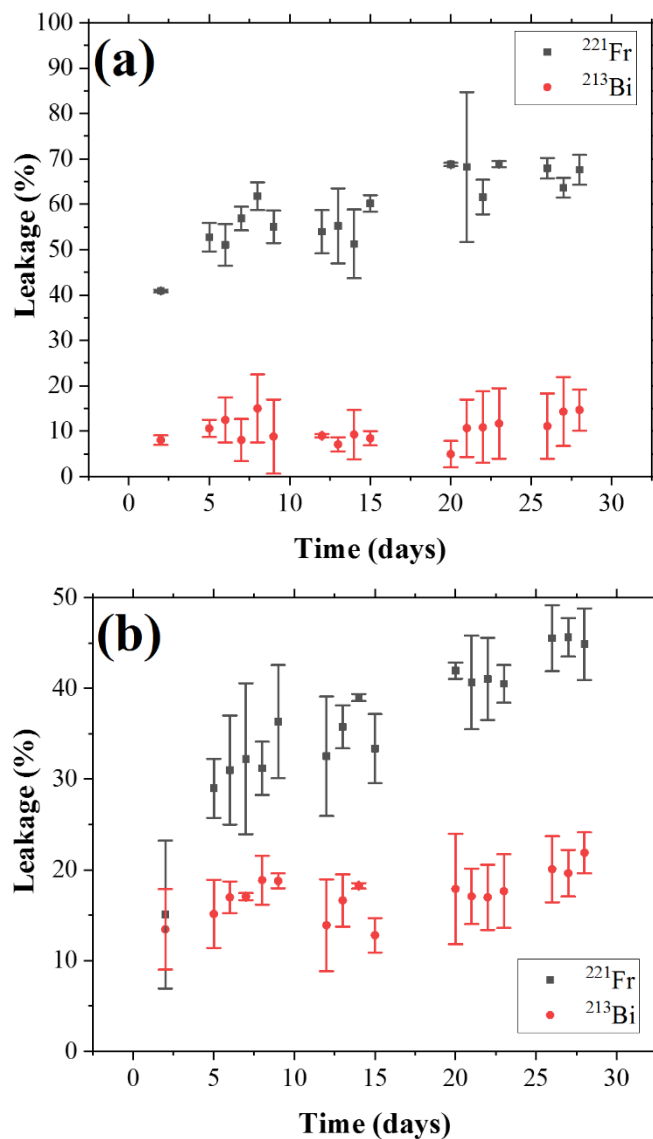


Fig. 7 Leakage of ^{221}Fr and ^{213}Bi from $\text{Gd}_{0.8}\text{Eu}_{0.2}\text{VO}_4$ (a) core and (b) core + 2 shells NPs as a function of time

4. Discussion

In this work, GdVO_4 NPs were doped with Eu^{3+} ions at concentrations of 5%–40% to assess their luminescence emission intensity. GdVO_4 was chosen as a host because of its efficient energy absorption and transfer as well as its chemical and thermal stability.^{3,21,23,26,27,63,70} Increasing the Eu^{3+} concentration in $\text{Gd}_{(1-x)}\text{Eu}_x\text{VO}_4$ core NPs caused a slight rise in the absorbance that is attributed to the $\text{Eu}^{3+}\text{-O}^{2-}$ charge transfer (250–260 nm), which was not observed due to overlapping with the $\text{V}^{5+}\text{-O}^{2-}$ band (Fig. S.2). The intensity of the $\text{Eu}^{3+}\text{-O}^{2-}$ excitation band (~280 nm) was greater for higher Eu^{3+} concentrations, where a significant difference was observed between samples except for 20% and 40% Eu^{3+} (Fig. S.3). Similarly, the emission intensity of $\text{Gd}_{(1-x)}\text{Eu}_x\text{VO}_4$ core NPs increased with higher Eu^{3+} concentrations up to 20%, where it reached a plateau since a negligible increase in intensity was

observed at 40% Eu^{3+} (Fig. S.4). The intensity results are consistent with $\text{Gd}_{(1-x)}\text{Eu}_x\text{VO}_4$ nanocrystals, where the highest luminescence intensity was observed at 25 mol% of Eu^{3+} .⁶⁶ The absolute quantum yield and the average luminescence decay lifetime decreased from 29.4% to 22.6% and 1.33 ms to 0.89 ms for $\text{Gd}_{0.95}\text{Eu}_{0.05}\text{VO}_4$ and $\text{Gd}_{0.6}\text{Eu}_{0.4}\text{VO}_4$, respectively (Tables S.5 and S.7). The plateau reached in the emission intensity and the decreased of the absolute quantum yield and average luminescence decay lifetime are related to the quenching observed at larger Eu^{3+} concentrations. Increasing the concentration of Eu^{3+} ions causes a decrease in the distance between dopant ions, which promotes Eu-Eu interactions resulting in cross relaxation processes.^{27,71,72} The higher the concentration of dopant ions, the greater is the probability of non-radiative de-excitation, which is observed as a decrease in the absolute quantum yield and average luminescence decay lifetime.⁶⁶ Additionally, the nonexponential behavior of the time-resolved luminescence decay curves may suggest the energy transfer of Eu^{3+} to impurities.⁶² The fact that $\text{Gd}_{0.95}\text{Eu}_{0.05}\text{VO}_4$ core NPs had the highest absolute quantum yield (29.4%) and longest average luminescence decay lifetime (1.33 ms) is consistent with the concentration quenching effect that has been reported for $[\text{Eu}^{3+}] > 5\%$.⁶³ Although the absolute quantum yield and average luminescence decay lifetime of $\text{Gd}_{0.8}\text{Eu}_{0.2}\text{VO}_4$ core NPs were 20.1% and 17.9% lower with respect to that of $\text{Gd}_{0.95}\text{Eu}_{0.05}\text{VO}_4$, a 20% Eu^{3+} concentration was used for the development of radionuclide-doped core and core-shell NPs. The selection of this concentration was based on the significant increase in emission intensity, which was 89% higher to that obtained for 5% Eu^{3+} .

The α -emitting radionuclide ^{225}Ac was chosen as a candidate to assess the retention capabilities of $\text{Gd}_{0.8}\text{Eu}_{0.2}\text{VO}_4$ NPs based on its potential as an “in vivo” generator for the treatment of micrometastases, solid tumors, and leukemia.⁷³ Its implementation has certain challenges associated to the leakage of decay daughters from the carrier due to recoil energy, which can cause unwanted *in vivo* radiotoxicity.³⁰ To improve the retention of decay daughters, two shells of $\text{Gd}_{0.8}\text{Eu}_{0.2}\text{VO}_4$ were deposited onto the core NPs as a dense atomic lattice barrier. An increase in the crystallite size was observed upon the deposition of two nonradioactive shells, which supports the formation of core-shell structures (Table 1). Low magnification TEM images for both core and core + 2 shells revealed the formation of aggregates, which could be attributed to the sample preparation and drying (Fig. S.5). An increase in the mean particle size is consistent with the results obtained for the crystallite size and supports the formation of core-shell structures. In addition, both $\text{Gd}_{0.8}\text{Eu}_{0.2}\text{VO}_4$ core and core + 2 shells NPs correspond to single crystals based on the similarities between the particle and crystallite size measured by x-ray diffraction. The increase in the polydispersity index and standard deviation suggest that new core NPs might be forming during the synthesis of core-shell structures and/or that NP aggregation is taking place (Table 2). The growth of new core NPs could be related to the high concentration of monomers used during the synthesis, which promotes homogeneous nucleation. The increase of both mean particle size and standard deviation supports the assumption that the formation of core-shell structures is due to Ostwald ripening.⁵⁸ Overall, the mean particle size obtained from both intensity and number distributions seems to overestimate the size of $\text{Gd}_{0.8}\text{Eu}_{0.2}\text{VO}_4$ core and core-shell NPs based on the magnitude of crystallite size and mean particle size measured by x-ray diffraction and TEM, respectively. The presence of citrate molecules on the surface or a counter ion layer in charged surfaces will contribute to an overestimation of the particle size from both size distributions. However, the larger hydrodynamic diameter and wider size distributions obtained based on the intensity distribution

suggests the aggregation of NPs upon the deposition of shells due to a lack of complexing agents (Fig. S.6).

The luminescence properties of core and core-shell NPs were characterized based on absorption, excitation, and emission spectra (Fig. 5) as well as the absolute quantum yield and average luminescence decay lifetime [Table. S.6 and Fig. S.7(b)]. The increment in the normalized absorbance intensity is related to a greater NP concentration in the core-shell suspensions due to their higher chemical yield with respect to core NPs [Fig. 5(a)]. A red shift in the excitation spectra and an increase in the intensity of the $O^{2-}-V^{5+}$ charge transfer band was observed after the deposition of shells to the core NPs [Fig. 5(b)]. The red shift implies that the core-shell structures could be excited with lower energy photons with respect to the core NPs. On the other hand, the increase in the $O^{2-}-V^{5+}$ charge transfer band suggests that the excitation of Eu^{3+} is more efficient through the $[VO_4]^{3-}$ units due to changes in the $Eu^{3+}-O^{2-}$ bond elongation and/or crystal cell volume for the core-shell NPs.^{62,74} These changes in the excitation spectra influenced the emission intensity of both core and core-shell NPs since the spectra were recorded using the same excitation wavelength ($\lambda_{ex} = 280$ nm). Hence, the lower emission intensity of both core-shell structures with respect to the core NPs is related to the use of an excitation wavelength that does not correspond to the maxima intensity (~ 310 nm) [Fig. 5(c)]. A decrease in the emission intensity could also be caused by NP aggregation in the case of both core-shell structures taking into account the dynamic light scattering results.⁷⁴ The absolute quantum yields were 22.8%, 18.5%, and 14.0% for $Gd_{0.8}Eu_{0.2}VO_4$ core, core + 1 shell, and core + 2 shells, respectively. As discussed above, the decrease in absolute quantum yield may be related to the conditions at which the emission spectra were collected. Briefly, the lower excitation intensity at 280 nm caused a decrease in the emission intensity and hence in the quantum yield of core-shell NPs. In addition, the aggregation of core-shell NPs could promote self-absorption of the Eu^{3+} emission by adjacent NPs. It is expected that the core-shell structures will have a similar quantum yield to that of core NPs based on the constant Eu^{3+} concentration (Table S.4). It is important to highlight that slight changes in quantum yield have been reported in lanthanide-based core-shell structures,⁷⁵ while depending on the shell composition an increase or decrease in magnitude can be obtained.⁷⁶ The average luminescence decay lifetime decreased 6.2% and 19.1% after deposition of 1 and 2 $Gd_{0.8}Eu_{0.2}VO_4$ shells, respectively. This decrease in the average luminescence decay lifetime may be associated to quenching effects promoted by impurities in the core-shell NPs. Therefore, the deposition of shells with the same lanthanide composition does not contribute to a reduction of the non-radiative de-excitation pathways as has been reported in lanthanide-based core-shell structures where the core and shell composition is different.⁷⁷ The magnetic susceptibility of both $Gd_{0.8}Eu_{0.2}VO_4$ core and core-shell NPs was $\sim 56 \times 10^{-6}$ emu Oe⁻¹ g⁻¹, since the lanthanide concentration remained constant (Table S.4). The synthesized NPs are expected to have a lower magnetic susceptibility with respect to pure $GdVO_4$ due to the presence of Eu^{3+} ions with lower effective magnetic moment based on the Curie-Weiss Law, where $(\mu_{eff})_{Eu} = 3.3-3.5 \mu_B$ and $(\mu_{eff})_{Gd} = 7.9-8.0 \mu_B$.⁷⁸ The lower magnetic susceptibility and concentration of Gd^{3+} ions may affect the response of $Gd_{0.8}Eu_{0.2}VO_4$ core-shell NPs as a positive (T_1) MRI contrast agent. Nonetheless, it has been demonstrated that replacing Gd^{3+} ions with Eu^{3+} enhances the proton relaxivities of the NPs with respect to pure $GdVO_4$ while giving luminescence functionalities.^{3,79}

The *in vitro* retention of ^{225}Ac and decay daughters, ^{221}Fr and ^{213}Bi , within $\text{Gd}_{0.8}\text{Eu}_{0.2}\text{VO}_4$ core and core + 2 shells NPs was assessed in this work. It is expected that the retention of ^{225}Ac cations in the NPs will be through the substitution of Ln^{3+} ions by ^{225}Ac in the crystal lattice because of their chemical similarities.³⁰ The leakage of ^{225}Ac from $\text{Gd}_{0.8}\text{Eu}_{0.2}\text{VO}_4$ core NPs may suggest that ^{225}Ac , due to its larger ionic radius relative to Gd^{3+} and Eu^{3+} , is not quantitatively retained in the crystal lattice. Additionally, the continuous increase in activity could only mean that ^{225}Ac is not a free ion but instead is in the form of a low-molecular-weight metal-citrate complex in solution⁸⁰ or adsorbed onto the NPs surface, which causes a slower transport through the dialysis membrane to that of free radionuclides (Fig. 6). The synthesis conditions used, heating time and temperature, may contribute to a lower consumption of the ^{225}Ac -citrate complexes as was evidenced by the chemical yield of core NPs. The ^{225}Ac radiochemical yield was $58.3 \pm 14.1\%$ for $\text{Gd}_{0.8}\text{Eu}_{0.2}\text{VO}_4$ core NPs, which is similar to the radiochemical yield of $47 \pm 5\%$ reported for LaPO_4 NPs of 3–5 nm after surface modification and purification.³⁰ The measured yield represents a significant enhancement with respect to procedures for radiolabeling monoclonal antibodies with ^{225}Ac that have shown $\sim 10\%$ of radiochemical yield.^{81,82} An increase to $94.8 \pm 1.5\%$ in the radiochemical yield was obtained after the deposition of two nonradioactive shells to $\text{Gd}_{0.8}\text{Eu}_{0.2}\text{VO}_4$ core NPs. This increase is attributed to two effects, (i) the higher chemical yield of core + 2 shells with respect to the core NPs and (ii) the retention of ^{225}Ac cations in the newly formed shells and/or core NPs during the core-shell synthesis procedure. It is presumed that ^{225}Ac -citrate complexes that do not result in core NP formation are consumed during the synthesis of core-shell structures. The longer heating times (>1 h) used for core-shell NPs synthesis contributed to the consumption of these species and hence to a reduction of ^{225}Ac leakage. As observed from core + 2 shells NPs, these ^{225}Ac -complexes were not completely consumed during the synthesis of the NPs. This is expected since citrate complexes are responsible for the stability of the NPs through complexation with surface Ln^{3+} ions. Although longer heating times (>30 minutes) and higher temperatures ($>60^\circ\text{C}$) can be used to increase the radiochemical yield and hence the retention of ^{225}Ac , large particle size and size distributions as well as a high probability of aggregation are expected. Lastly, it is important to highlight that the tetragonal crystal structure, characteristic of LnVO_4 , has proven to be suitable for the immobilization of actinides with a tetravalent state.⁸³

The leakage of ^{221}Fr from core NPs was $40.9 \pm 0.3\%$ after 2 days and increased to $67.6 \pm 3.3\%$ following 28 days in dialysis [Fig. 7(a)]. This result is higher with respect to the 60% and 40% leakage of ^{221}Fr reported for LaPO_4 and $\text{La}_{0.5}\text{Gd}_{0.5}\text{PO}_4$ core NPs, respectively.^{30,32} The deposition of two nonradioactive shells to the core NPs decreases the leakage of ^{221}Fr to $45.5 \pm 3.6\%$. This enhancement is consistent with the *in vitro* retention results of $\text{La}_{0.5}\text{Gd}_{0.5}\text{PO}_4$ and LaPO_4 core + 2 shells NPs containing ^{225}Ac , which showed an increase in the retention of ^{221}Fr to 70% and 80%, respectively.^{29,32} Retention of ^{213}Bi was higher to that of ^{221}Fr , having $<15\%$ and $\sim 22\%$ leakage from core and core + 2 shells NPs, respectively (Fig. 7). Considering the published data on fate of ^{221}Fr and ^{213}Bi in lanthanum phosphate systems,^{30–32} we strongly believe that the citrate groups present on the surface of $\text{Gd}_{0.8}\text{Eu}_{0.2}\text{VO}_4$ core-shell NPs were responsible for the lower ^{213}Bi leakage with respect to that of ^{221}Fr . The recoiled ^{213}Bi ions out of the NPs are thermalized quickly (within ~ 30 nm) and may form a complex with the citrate groups on the surface of $\text{Gd}_{0.8}\text{Eu}_{0.2}\text{VO}_4$ NPs. Therefore, the formation of Bi-citrate complexes resulted in an apparent increase in the retention of ^{213}Bi (i.e. lower concentration of Bi in the dialysate). This hypothesis was supported by an experiment, where $\text{Gd}_{0.8}\text{Eu}_{0.2}\text{VO}_4$ core and core

+ 2 shells NPs were mixed with BiCl₃ and dialyzed against DI water, in which somewhat higher retention of Bi ions was obtained by core relative to core + 2 shells NPs. Briefly, Gd_{0.8}Eu_{0.2}VO₄ core and core + 2 shells NPs were synthesized as reported in the experimental section. The NPs suspensions (400 μL) were mixed with BiCl₃ (20 μL of 0.5 M). The suspension was then dialyzed against DI water and aliquots from the dialysate were taken periodically (0.5, 1, 2, 4, 24, and 47 h). The aliquots were characterized using ICP-OES to assess the concentration of Bi in the dialysate. The results are summarized in Table S.9, where a 100% leakage of Bi would result in a Bi concentration of ~10.4 μg/mL in the dialysate. As shown in Table S.9, overall, the leakage of Bi from core + 2 shells was higher than that from core NPs. The concentration of citrate groups on the surface of Gd_{0.8}Eu_{0.2}VO₄ core-shell NPs and in solution by far exceeds the concentration of ²¹³Bi ions, which is well below nanomolar range. The suggested mechanism is consistent with the lower retention of ²¹³Bi ions by Gd_{0.8}Eu_{0.2}VO₄ core + 2 shells NPs with respect to that of core, having a lower fraction of citrate groups on the surface due to the longer heating times used (>1 h). Note that ranges of ²²¹Fr and ²¹³Bi in GdVO₄, with a crystal density (ρ) of 5.47 g/cm³, are ~26 and ~30 nm, respectively (corresponding to recoil energies of 105.5 and 132.8 keV, respectively, calculated from classical conservation of momentum). Due to the similarity of ranges of ²²¹Fr and ²¹³Bi ions in NPs and the size of the NPs, one can expect that all ²²¹Fr and ²¹³Bi ions should leak out of the NPs. The partial retention of ²²¹Fr and ²¹³Bi ions, however, may be attributed to the fact the inorganic NPs are very rigid, and it is conceivable that a fraction of the recoil energy is transferred to the translational energy of NPs, i.e. the recoil energy is reduced by $[m_{\text{Fr}}/(m_{\text{Fr}}+m_{\text{NP}})]$, where m_{Fr} is atomic mass of francium and m_{NP} is the average molecular mass of NP, which is ~1000 (a similar argument holds for ²¹³Bi).

Although the deposition of two shells to the radioactive Gd_{0.8}Eu_{0.2}VO₄ core NPs improved the retention of decay daughters, further steps are required to decrease the release of ²²¹Fr and ²¹³Bi. For example, the deposition of more than two nonradioactive shells with the same composition to the core NPs could provide a thicker barrier and hence improve the retention of radionuclides.³² Deposition of shells with different composition to that of the radioactive core NPs not only would enhance the retention of decay daughters, but it will also provide multifunctional capabilities to the core-shell NPs. The deposition of a gold shell to the core-shell NPs is an alternative to minimize leakage of ²²¹Fr owing to the higher stopping power of gold.⁸⁴ This gold shell could also facilitate the functionalization and antibody conjugation of the NPs for *in vivo* biodistribution and retention studies. Gd_{0.8}Eu_{0.2}VO₄ core and core + 2 shells NPs represent an alternative to LnPO₄ core-shell NPs,^{29–33,35} liposomes,^{9,85–88} polymersomes,^{10,84,89} and various inorganic NPs,^{90–92} among others, for the encapsulation of ²²⁵Ac, decay daughters, and other therapeutically relevant radionuclides. The main advantages of Gd_{0.8}Eu_{0.2}VO₄ core-shell NPs as carriers for TAT are related to their synthetic procedure and their intrinsic properties for multimodal molecular imaging. The proposed synthesis route allows the development of monodisperse LnVO₄ NPs with a particle size below 10 nm and a tetragonal crystal system at moderate temperatures (<90°C) and a short synthesis time (<1 h).^{3,55} The small particle size of LnVO₄ NPs may contribute to a beneficial biodistribution and clearance for *in vivo* applications with respect to that expected for either polymersomes or liposomes having similar retention of decay daughters, which requires sizes larger than 100 nm.⁶⁹ Both liposomes and polymersomes will require the addition of either a fluorescence dye or Gd-chelate to obtain multimodal imaging capabilities. Labeling both polymer vesicles with compounds for fluorescence and magnetic resonance imaging will involve additional procedures and may also

affect or compromise the retention of radionuclides. Similarly, functionalized TiO₂ NPs doped with ²²⁵Ac will require the addition of dyes or magnetic agents to provide multimodal imaging functionalities in the same carrier. The relatively short time required for the formation of LnVO₄ core NPs would be an advantage with respect to LnPO₄ NPs for the implementation of short-lived radionuclides for diagnostic and/or therapeutic applications.

5. Conclusions

Europium-doped GdVO₄ NPs were synthesized using an aqueous route based on the precipitation of Ln³⁺ and [VO₄]³⁻ with sodium citrate as a complexing agent and varying the concentration of Eu³⁺ ions. A Eu³⁺ concentration of 20% had the highest normalized luminescence emission among the evaluated concentrations. Successful deposition of Gd_{0.8}Eu_{0.2}VO₄ shells was achieved by mixing a solution containing lanthanide-citrate-vanadate complexes with the Gd_{0.8}Eu_{0.2}VO₄ core NPs suspensions followed by heating at 60°C for 30 minutes. Monodisperse NPs with a tetragonal crystal structure and a mean particle size of 6.1 ± 1.4 nm and 12.4 ± 2.0 nm were obtained for core and core + 2 shells, respectively. *In vitro* retention of ²²⁵Ac, ²²¹Fr, and ²¹³Bi was studied to assess the potential application of Gd_{0.8}Eu_{0.2}VO₄ core and core + 2 shells as radionuclide carriers. Radiochemical yield of ²²⁵Ac increased from 58.3 ± 14.1% to 94.8 ± 1.5% upon deposition of two nonradioactive shells onto Gd_{0.8}Eu_{0.2}VO₄ core NPs. The leakage of ²²¹Fr from core NPs reached a maximum of 67.6 ± 3.3% after 28 days in dialysis, while for core + 2 shells it was 45.5 ± 3.6%. The range of decay daughters in GdVO₄ (26–30 nm) is expected to be the main reason for ²²¹Fr and ²¹³Bi leakage from core and core + 2 shells NPs. Improvement of retention capabilities of decay daughters can be achieved by depositing a greater number of shells onto the core NPs with same or different composition (*i.e.* gold or silica). Gd_{0.8}Eu_{0.2}VO₄ core + 2 shells NPs have potential as multimodal fluorescence, magnetic resonance, and nuclear imaging contrast agents as well as platforms for targeted alpha therapy.

Acknowledgments

This work was financed by the Virginia Commonwealth University (VCU) with the support of the Mechanical and Nuclear Engineering Department and NRC-HQ-84-14-FOA-002, Faculty Development Program in Radiation Detection and Health Physics at VCU. Work at ORNL was supported in part by (i) the U.S. Department of Energy Isotope Program within the Office of Nuclear Physics and (ii) an appointment to the Oak Ridge National Laboratory Nuclear Engineering Science Laboratory Synthesis Program, sponsored by the US Department of Energy and administered by the Oak Ridge Institute for Science and Education. We would like to thank the staff of Nuclear and Radiochemistry Group at ORNL for their help with radiochemistry and radioactivity measurement. The authors also wish to thank Dr. Joseph Turner from the Instrumentation Laboratory in the Department of Chemistry at VCU, the staff at the Nanomaterials Core Characterization Facility in the VCU College of Engineering and Dr. Gary Tepper's Laboratory their assistance with fluorescence measurements and nanomaterials characterization.

Conflicts of Interest

There are no conflicts to declare.

References

- 1 Z. Liu, F. Kiessling and J. Gätjens, *J. Nanomater.*, 2010, **2010**, 894303.
- 2 P. Padmanabhan, A. Kumar, S. Kumar, R. K. Chaudhary and B. Gulyás, *Acta Biomater.*, 2016, **41**, 1–16.
- 3 M. Abdesselem, M. Schoeffel, I. Maurin, R. Ramodiharilafy, G. Autret, O. Clément, P. L. Tharaux, J. P. Boilot, T. Gacoin, C. Bouzigues and A. Alexandrou, *ACS Nano*, 2014, **8**, 11126–11137.
- 4 S. K. Murthy, *Int. J. Nanomedicine*, 2007, **2**, 129–41.
- 5 S. Nazir, T. Hussain, A. Ayub, U. Rashid and A. J. MacRobert, *Nanomedicine Nanotechnology, Biol. Med.*, 2014, **10**, 19–34.
- 6 S. Bhattacharyya, R. Kudgus and R. Bhattacharya, *Pharm. Res.*, 2011, **28**, 237–259.
- 7 N. Nasongkla, E. Bey, J. Ren, H. Ai, C. Khemtong, J. S. Guthi, S. F. Chin, A. D. Sherry, D. A. Boothman and J. Gao, *Nano Lett.*, 2006, **6**, 2427–2430.
- 8 C. Oerlemans, W. Bult, M. Bos, G. Storm, J. F. W. Nijsen and W. E. Hennink, *Pharm. Res.*, 2010, **27**, 2569–2589.
- 9 G. Henriksen, B. W. Schoultz, T. E. Michaelsen, S. Bruland and R. H. Larsen, *Nucl. Med. Biol.*, 2004, **31**, 441–449.
- 10 G. Wang, R. M. De Kruijff, A. Rol, L. Thijssen, E. Mendes, A. Morgenstern, F. Bruchertseifer, M. C. A. Stuart, H. T. Wolterbeek and A. G. Denkova, *Appl. Radiat. Isot.*, 2014, **85**, 45–53.
- 11 Y. Zheng, F. Fu, M. Zhang, M. Shen, M. Zhu and X. Shi, *Med. Chem. Commun.*, 2014, **5**, 879–885.
- 12 P. Zrazhevskiy, M. Sena and X. Gao, *Chem. Soc. Rev.*, 2010, **39**, 4326.
- 13 S. J. Kennel, J. D. Woodward, A. J. Rondinone, J. Wall, Y. Huang and S. Mirzadeh, *Nucl. Med. Biol.*, 2008, **35**, 501–514.
- 14 J. D. Woodward, S. J. Kennel, S. Mirzadeh, S. Dai, J. S. Wall, T. Richey, J. Avenell and A. J. Rondinone, *Nanotechnology*, 2007, **18**, 5.
- 15 A. J. Mieszawska, W. J. M. Mulder, Z. A. Fayad and D. P. Cormode, *Mol. Pharm.*, 2013, **10**, 831–847.
- 16 D. Hoffman, M. Sun, L. Yang, P. R. McDonagh, F. Corwin, G. Sundaresan, L. Wang, V. Vijayaragavan, C. Thadigiri, N. Lamichhane and J. Zweit, *Am. J. Nucl. Med. Mol. Imaging*, 2014, **4**, 548–60.
- 17 X. Kang, A. Dongmei Yang, A. Yunlu Dai, A. Mengmeng Shang, A. Ziyong Cheng, X. Zhang, H. Lian, A. Ma and J. Lin, *Nanoscale*, 2013, **5**, 253–2261.
- 18 C. Bouzigues, T. Gacoin and A. Alexandrou, *ACS Nano*, 2011, **5**, 8488–8505.
- 19 Y. Zhang, W. Wei, G. K. Das and T. T. Yang Tan, *J. Photochem. Photobiol. C Photochem. Rev.*, 2014, **20**, 71–96.
- 20 H. Dong, S.-R. Du, X.-Y. Zheng, G.-M. Lyu, L.-D. Sun, L.-D. Li, P.-Z. Zhang, C. Zhang and C.-H. Yan, *Chem. Rev.*, 2015, **115**, 10725–10815.
- 21 A. Szczeszak, A. Ekner-Grzyb, M. Runowski, L. Mrówczyńska, T. Grzyb and S. Lis, *J. Nanoparticle Res.*, 2015, **17**, 11.
- 22 Q. Du, Z. Huang, Z. Wu, X. Meng, G. Yin, F. Gao and L. Wang, *Dalt. Trans*, 2015, **44**, 3934–3940.
- 23 S. Huang, Z. Cheng, A. Ma, X. Kang, Y. Dai and J. Lin, *Dalt. Trans.*, 2013, **42**, 6523–6530.

- 24 Y. Liu, G. Liu, X. Dong, J. Wang and W. Yu, *Phys. Chem. Chem. Phys. Phys. Chem. Chem. Phys.*, 2015, **17**, 26638–26644.
- 25 W. Xu, J. Y. Park, K. Kattel, B. A. Bony, W. C. Heo, S. Jin, J. W. Park, Y. Chang, J. Y. Do, K. S. Chae, T. J. Kim, J. A. Park, Y. W. Kwak and G. H. Lee, *New J. Chem.*, 2012, **36**, 2361.
- 26 T. Kim, N. Lee, Y. Il Park, J. Kim, J. Kim, E. Y. Lee, M. Yi, B.-G. Kim, T. Hyeon, T. Yu and H. Bin Na, *RSC Adv.*, 2014, **4**.
- 27 N. O. Nuñez, S. Rivera, D. Alcantara, J. M. de la Fuente, J. García-Sevillano and M. Ocaña, *Dalton Trans.*, 2013, **42**, 10725–34.
- 28 R. D. Teo, J. Termini and H. B. Gray, *J. Med. Chem.*, 2016, acs.jmedchem.5b01975.
- 29 J. V. Rojas, J. D. Woodward, N. Chen, A. J. Rondinone, C. H. Castano and S. Mirzadeh, *Nucl. Med. Biol.*, 2015, **42**, 614–620.
- 30 J. Woodward, S. J. Kennel, A. Stuckey, D. Osborne, J. Wall, A. J. Rondinone, R. F. Standaert and S. Mirzadeh, *Bioconjug. Chem.*, 2011, **22**, 766–776.
- 31 M. F. McLaughlin, J. Woodward, R. A. Boll, J. S. Wall, A. J. Rondinone, S. J. Kennel, S. Mirzadeh and J. D. Robertson, *PLoS One*, 2013, **8**, 2–9.
- 32 B. M. F. McLaughlin, J. Woodward, R. A. Boll, A. J. Rondinone, S. Mirzadeh and J. D. Robertson, *Radiochim.*, 2013, **101**, 595–600.
- 33 M. F. McLaughlin, D. Robertson, P. H. Pevsner, J. S. Wall, S. Mirzadeh and S. J. Kennel, *Cancer Biother. Radiopharm.*, 2014, **29**, 34–41.
- 34 B. I. Kharisov, O. V. Kharissova and S. S. Berdonosov, *Recent Pat. Nanotechnol.*, 2014, **8**, 79–96.
- 35 N. Sobol, L. Sutherlin, E. Cedrowska, J. Schorp, C. Rodríguez-Rodríguez, J. Lattimer, D. C. Miller, P. Pevsner and J. D. Robertson, *APL Bioeng.*, 2018, **2**, 016101.
- 36 X. Zhang, J. Ge, Y. Xue, B. Lei, D. Yan, N. Li, Z. Liu, Y. Du and R. Cai, *Chem. - A Eur. J.*, 2015, **21**, 11954–11960.
- 37 L. Yang, G. Sundaresan, M. Sun, P. Jose, D. Hoffman, P. R. McDonagh, N. Lamichhane, C. S. Cutler, J. M. Perez and J. Zweit, *J. Mater. Chem. B*, 2013, **1**, 1421–1431.
- 38 P. R. McDonagh, G. Sundaresan, L. Yang, M. Sun, R. Mikkelsen and J. Zweit, *Nanomedicine Nanotechnology, Biol. Med.*, 2018, **14**, 1429–1440.
- 39 M. Toro-Gonzalez, D. M. Clifford, R. Copping, S. Mirzadeh and J. V. Rojas, *J. Nanoparticle Res.*, 2018, **20**, 238.
- 40 T. V. Gavrilovic, D. J. Jovanovic, K. Smits and M. D. Dramicanin, *Dye. Pigment.*, 2016, **126**, 1–7.
- 41 Y. Yan, J. Wang, M. Hojamberdiev, Z. Lu, B. Ren and Y. Xu, *J. Alloys Compd.*, 2014, **597**, 282–290.
- 42 P. Kumari and J. Manam, *J. Mater. Sci. Mater. Electron.*, 2016, **27**, 9437–9447.
- 43 N. Shanta Singh, R. S. Ningthoujam, G. Phaomei, S. D. Singh, A. Vinu and R. K. Vatsa, *Dalton Trans.*, 2012, **41**, 4404–12.
- 44 J. H. Oh, B. K. Moon, B. C. Choi, J. H. Jeong, J. H. Kim and H. S. Lee, *Solid State Sci.*, 2015, **42**, 1–5.
- 45 T. Grzyb, A. Gruszczyka, R. J. Wiglusz, Z. Śniadecki, B. Idzikowski and S. Lis, *J. Mater. Chem.*, 2012, **22**, 22989.
- 46 B. Stephan Heer, K. Kömpe, H.-U. Güdel, M. Haase, M. Haase, K. Kömpe, S. Heer and H. Güdel, *Adv. Mater.*, 2004, **16**, 2102–2105.
- 47 X. Wang, Y. E. Wang, J. Yu, Y. Bu and X. Yan, *Opt. Express*, 2018, **26**, 21950–21959.

- 48 X. Wang, T. Xu, P. Cai, T. Vu and H. J. Seo, *J. Alloys Compd.*, 2017, **691**, 530–536.
- 49 W. Yin, L. Zhou, Z. Gu, G. Tian, S. Jin, L. Yan, X. Liu, G. Xing, W. Ren, F. Liu, Z. Pan and Y. Zhao, *J. Mater. Chem.*, 2012, **22**, 6974.
- 50 H. Wang and L. Wang, *Inorg. Chem.*, 2013, **52**, 2439–2445.
- 51 A. A. Ansari, J. P. Labis and S. A. H. Alrokayan, *J. Nanoparticle Res.*, 2012, **14**, 999.
- 52 J. W. Stouwdam, M. Raudsepp and F. C. J. M. Van Veggel, *Langmuir*, 2005, **21**, 7003–7008.
- 53 J. Hu and Q. Wang, *Mater. Lett.*, 2014, **120**, 20–22.
- 54 F. Goubard, P. Griesmar and A. Tabuteau, *J. Solid State Chem.*, 2005, **178**, 1898–1902.
- 55 A. Huignard, V. Buissette, G. Laurent, T. Gacoin and J. P. Boilot, *Chem. Mater.*, 2002, **14**, 2264–2269.
- 56 R. A. Boll, D. Malkemus and S. Mirzadeh, *Appl. Radiat. Isot.*, 2005, **62**, 667–679.
- 57 V. K. Lamer and R. H. Dinegar, *J. Am. Chem. Soc.*, 1950, **72**, 4847–4854.
- 58 P. W. Voorhees, *J. Stat. Phys.*, 1985, **38**, 231–252.
- 59 S. Cotton, *Lanthanide and Actinide Chemistry*, Jhon Wiley & Sons, 1 Ed., 2006.
- 60 S. Blundell, *Magnetism in Condensed Matter*, Oxford University Press, Oxford, 1 Ed., 2001.
- 61 V. Singh, S. Takami, N. Aoki, D. Hojo, T. Arita and T. Adschiri, *J. Nanoparticle Res.*, 2014, **16**, 2378.
- 62 A. Szczeszak, T. Grzyb, Z. Niadecki, N. Andrzejewska, S. Lis, M. Matczak, G. Nowaczyk, S. Jurga and B. Idzikowski, *Inorg. Chem.*, 2014, **53**, 12243–12252.
- 63 Z. Zhou, G. Li and P. Jia, *Rare Met. Mater. Eng.*, 2014, **43**, 1588–1593.
- 64 J. R. Lakowicz, Ed., *Principles of Fluorescence Spectroscopy*, Springer US, Boston, MA, 2006.
- 65 X. Su, B. Yan and H. Huang, *J. Alloys Compd.*, 2005, **399**, 251–255.
- 66 V. Muhr, M. Buchner, T. Hirsch, D. J. Jovanovi, S. D. Doli, M. D. Dramianin and O. S. Wolfbeis, *Sensors Actuators, B Chem.*, 2017, **241**, 349–356.
- 67 J.-C. Boyer and F. C. J. M. van Veggel, *Nanoscale*, 2010, **2**, 1417.
- 68 N. Yaiphaba, R. S. Ningthoujam, N. S. Singh, R. K. Vatsa, N. R. Singh, S. Dhara, N. L. Misra and R. Tewari, *J. Appl. Phys.*, 2010, **107**, 034301.
- 69 R. M. de Kruijff, H. T. Wolterbeek and A. G. Denkova, *Pharmaceuticals*, 2015, **8**, 321–336.
- 70 T. V. Gavrilović, D. J. Jovanović, V. Lojpur and M. D. Dramićanin, *Sci. Rep.*, 2014, **4**, 4209.
- 71 K. Riwozki and M. Haase, *J. Phys. Chem. B*, 1998, **102**, 10129–10135.
- 72 A. Huignard, T. Gacoin and J.-P. Boilot, *Chem. Mater.*, 2000, **12**, 1090–1094.
- 73 A. B. J., *J Biomed Phys Eng*, 2013, **3**, 67–80.
- 74 N. S. Singh, R. S. Ningthoujam, N. Yaiphaba, S. D. Singh and R. K. Vatsa, *J. Appl. Phys.*, 2009, **105**, 064303.
- 75 V. Buissette, M. Moreau, T. Gacoin and J.-P. Boilot, *Adv. Funct. Mater.*, 2006, **16**, 351–355.
- 76 K. Kömpe, H. Borchert, J. Storz, A. Lobo, S. Adam, T. Möller and M. Haase, *Angew. Chemie - Int. Ed.*, 2003, **42**, 5513–5516.
- 77 J.-C. Zhou, L.-D. Sun, J. Shen, J.-Q. Gu and C.-H. Yan, *Nanoscale*, 2011, **3**, 1977.
- 78 W. Xu, K. Kattel, J. Y. Park, Y. Chang, T. J. Kim, G. H. Lee, T. Erpelding, A. H. Schmieder, G. Kiefer, G. Gulyas, P. S. Athey, P. J. Gaffney, S. A. Wickline, G. M. Lanza

- and G. H. Lee, *Phys. Chem. Chem. Phys.*, 2012, **14**, 12687.
- 79 C.-Y. Chou, M. Abdesselem, C. Bouzigues, M. Chu, A. Guiga, T.-H. Huang, F. Ferrage, T. Gacoin, A. Alexandrou and D. Sakellariou, *Sci. Rep.*, 2017, **7**, 44770.
- 80 D. A. Scheinberg and M. R. McDevitt, *Curr. Radiopharm.*, 2011, **4**, 306–320.
- 81 M. R. Mcdevitt, D. Ma, J. Simon, R. K. Frank and D. A. Scheinberg, *Appl. Radiat. Isot.*, 2002, **57**, 841–847.
- 82 W. F. Maguire, M. R. McDevitt, P. M. Smith-Jones and D. A. Scheinberg, *J. Nucl. Med.*, 2014, **55**, 1492–8.
- 83 S. Neumeier, Y. Arinicheva, Y. Ji, J. M. Heuser, P. M. Kowalski, P. Kegler, H. Schlenz, D. Bosbach and G. Deissmann, *Radiochim. Acta*, 2017, **105**, 961–984.
- 84 R. M. De Kruijff, K. Drost, L. Thijssen, A. Morgenstern, F. Bruchertseifer, D. Lathouwers, H. T. Wolterbeek and A. G. Denkova, *Appl. Radiat. Isot.*, 2017, **128**, 183–189.
- 85 S. Sofou, J. L. Thomas, H.-Y. Lin, M. R. Mcdevitt, D. A. Scheinberg and G. Sgouros, *J. Nucl. Med.*, 2004, **45**, 253–260.
- 86 S. Sofou, B. J. Kappel, J. S. Jaggi, M. R. Mcdevitt, D. A. Scheinberg and G. Sgouros, *Bioconjug. Chem.*, 2007, **18**, 2061–2067.
- 87 M.-Y. Chang, J. Seideman and S. Sofou, *Bioconjug. Chem.*, 2008, **19**, 1274–1282.
- 88 T. J. Jonasdottir, D. R. Fisher, J. Borrebæk, Ø. S. Bruland and R. H. Larsen, *Anticancer Res.*, 2006, **26**, 2841–2848.
- 89 L. Thijssen, D. R. Schaart, D. de Vries, A. Morgenstern, F. Bruchertseifer and A. G. Denkova, *Radiochim. Acta*, 2012, **100**, 473–482.
- 90 E. Cędrowska, M. Pruszynski, A. Majkowska-Pilip, S. Męczyńska-Wielgosz, F. Bruchertseifer, A. Morgenstern and A. Bilewicz, *J. Nanoparticle Res.*, 2018, **20**, 83.
- 91 A. Piotrowska, S. Męczyńska-Wielgosz, A. Majkowska-Pilip, P. Koźmiński, G. Wójciuk, E. Cędrowska, F. Bruchertseifer, A. Morgenstern, M. Kruszewski and A. Bilewicz, *Nucl. Med. Biol.*, 2017, **47**, 10–18.
- 92 A. Piotrowska, E. Leszczuk, F. Bruchertseifer, A. Morgenstern and A. Bilewicz, *J. Nanoparticle Res.*, 2013, **15**, 1–11.